ROYAL SOCIETY
OF CHEMISTRY

## PAPER

Check for updates

# An eco-friendly gelatin based triboelectric nanogenerator for a self-powered PANI nanorod/NiCo$_2$O$_4$ nanosphere ammonia gas sensor†

Dongzhi Zhang, [ID] * Yan Yang, Zhenyuan Xu, Dongyue Wang and Chen Du

It is of great significance to develop low-cost, eco-friendly backup power sources for driving gas sensors. In this work, a gas sensor based on the PANI/NiCo$_2$O$_4$ composite was driven by a gelatin-polyimide based triboelectric nanogenerator (GP-TENG) for the detection of NH$_3$ at room temperature. Nanostructured gelatin films prepared with abrasive paper as the template dramatically enhanced the output performance of the GP-TENG and showed excellent degradability in water. The peak-to-peak voltage of the GP-TENG could reach 400 V, and the output power could reach 6.16 mW. The GP-TENG could not only drive low-powered electronic devices such as LEDs and calculators, but also could perform motion detection, such as finger touch, elbow bending, *etc.* A circuit module of rectification and voltage regulation was designed to convert AC voltage from the GP-TENG into stable 24 V DC voltage, which could provide constant voltage input for the gas sensor. The GP-TENG, the circuit module of rectification and voltage regulation, and the PANI/NiCo$_2$O$_4$ gas sensor were integrated to construct a GP-TENG-driven ammonia gas sensor (GPAS). The GPAS exhibits excellent response ($V_g/V_a$ = 467% @20 ppm) towards NH$_3$ sensing, and also shows good repeatability, selectivity and long-term stability. This work provides an eco-friendly and economical solution to fabricate a reliable backup power source to achieve self-powered function for NH$_3$ gas sensors, which paves the way for the construction of a "smart factory" in the future.

## 1. Introduction

Ammonia (NH$_3$) is a colorless and toxic gas with a strong pungent smell.[1] It is widely used in the fields of agricultural production, pharmaceuticals and synthetic fibers and has a tremendous application value.[2–4] However, the leakage problem of NH$_3$ is inevitable. Long-term exposure to NH$_3$ could burn the skin, eyes and mucous membranes of respiratory organs, which can even lead to death when humans inhale too much NH$_3$ at one time.[5] Hence, it is essential to achieve rapid and accurate detection of NH$_3$. With the fast growth of Internet of Things (IoT) technology, the sensing unit is gradually developing in the direction of wireless, portability, miniaturization, multifunction and low power consumption.[6] At present, conventional NH$_3$ sensors need an additional power source, which can't meet the above-mentioned requirements.[7] Therefore, it is of vital importance to develop a self-powered NH$_3$ sensor.

The phenomenon of friction is very common in our daily life. Easily overlooked behaviors such as walking and arm swinging can cause friction.[8] In 2012, Z. L. Wang's group presented the idea of triboelectric nanogenerators (TENGs), which could convert the disorderly and irregular energy scattered in the environment into effective electricity.[9] So far, TENGs have great potential in three major application fields. First, TENGs are used as a micro-nano energy source. TENGs could be used to harvest energy generated by raindrops and be applied in cardiac pacemakers.[10,11] Secondly, TENGs are used for self-powered sensing. The measurement of various physical/chemical parameters can be achieved through detecting the voltage or current signals of TENGs.[12–15] Thirdly, TENGs are used as blue energy, which could harvest ocean wave energy. It is a promising sustainable energy technology for the future.[16,17] Up to now, numerous excellent self-powered gas sensors driven by TENGs have been reported. Su *et al.* prepared a variety of self-powered gas sensors to detect NO$_2$, NH$_3$, C$_3$H$_6$O and other gases, which exhibited brilliant gas-sensing performance.[18–21] Therefore, it is feasible to utilize TENGs to drive gas sensors to realize self-powered capability.

The selection of friction materials is the most critical step in preparation of TENGs.[22] However, extensively used friction materials of TENGs are polymers including poly(tetrafluoroethylene) (PTFE), poly(vinylidene fluoride) (PVDF), and metals

*College of Control Science and Engineering, China University of Petroleum (East China), Qingdao 266580, China. E-mail: dzzhang@upc.edu.cn; Fax: +86-532-86981335; Tel: +86-532-86982928*

† Electronic supplementary information (ESI) available. See https://doi.org/10.1039/d2ta01788a

This journal is © The Royal Society of Chemistry 2022

*J. Mater. Chem. A*, 2022, **10**, 10935–10949 | **10935**

including copper and aluminum.[23] These materials are expensive and non-degradable, which greatly limits their practical application. Therefore, it is imperative to seek a cheap, lightweight and degradable friction material to replace the aforementioned materials. Gelatin is a transparent, colorless and unscented macromolecular hydrocolloid. It is obtained by processing collagen extracted from bones and skins of animals, which is extensively used as an excipient and thickener in the food industry.[24,25] Gelatin holds advantages of inexpensiveness, biocompatibility and degradability. It is also rich in amino acid residues with electron donor groups, which can serve as electron donors and give gelatin potent capability to lose electrons during the process of contact and separation.[26] As a result, gelatin is an ideal positive friction material. Besides, modification of the surface of selected friction materials is an effective means to improve the performance of TENGs.[27] The increase in surface roughness through preparing nano/micro patterns on friction materials could improve the effective contact area.[28] Numerous techniques are applied to increase the surface roughness of friction materials, such as electrospinning, etching, plasma treatment and so on.[29–31]

In this paper, a self-powered $NH_3$ gas sensor based on the $PANI/NiCo_2O_4$ composite was fabricated in order to obtain a gas sensor that could still detect the $NH_3$ concentration on some occasions when the power source couldn't work, and at the same time to implement the concept of national vigorous development of new energy. A backup power source (GP-TENG) was designed. Nanostructured gelatin films and polyimide (PI) films worked together to build a multifunctional, inexpensive, and eco-friendly gelatin-polyimide based triboelectric nanogenerator (GP-TENG). In order to provide stable voltage input for the gas sensor, a circuit module of rectification and voltage regulation was designed to convert the AC voltage of the GP-TENG to a 24 V DC voltage signal. The GP-TENG, the circuit module of rectification and voltage regulation, and the $PANI/NiCo_2O_4$ gas sensor were integrated to build a GP-TENG-driven ammonia sensor (GPAS). The GPAS could be applied to continuous and uninterrupted vibration occasions such as engine vibration and the flow of exhaust gas in factories. When the power source works normally, the $NH_3$ concentration is monitored by detecting the resistance signal of the gas sensor. When the power source fails to work normally, the backup power source (GP-TENG) drives the gas sensor to continue to work, and the gas concentration could still be monitored by detecting the voltage signal across the two ends of the gas sensor. The GPAS has great practical application prospects in the future.

## 2. Experimental section

### 2.1. Materials

Cobalt(II) acetate tetrahydrate ($Co(CH_3COO)_2 \cdot 4H_2O$) was from Macklin Biochemical Co., Ltd. Polyimide (PI) films were obtained from a local market (thickness of 0.025 mm). Abrasive paper of different grades was obtained from MATADOR Co., Ltd. Double-sided copper foil tapes were purchased from 3 M Co., Ltd (thickness of 0.065 mm). Gelatin granules, nickel(II)

acetate tetrahydrate ($Ni(CH_3COO)_2 \cdot 4H_2O$), ammonium bicarbonate ($NH_4HCO_3$), ethylene glycol, ammonium persulphate (APS), aniline ($C_6H_7N$) and hydrochloric acid (HCl) were from Sinopharm Chemical Reagent.

### 2.2. Preparation of nanostructured gelatin films

The open circuit voltage ($V_{oc}$) generated by the smooth gelatin film and the PI film is pretty low. Through preliminary investigation, it was found that increasing the surface roughness of friction materials can enhance the effective contact area, thereby improving the output performance of the TENG.[32] Therefore, abrasive paper of various meshes was used as the template to prepare gelatin films with different rough surfaces by a spin-coating technique.

First, 1 g of gelatin granules was added to 20 mL deionized water and agitated at 60 °C for 0.5 h until gelatin granules were completely dissolved, at which point light yellow colloids were formed. Then, the obtained colloids were uniformly coated on abrasive paper of different meshes *via* the spin-coating method. After that, abrasive paper with gelatin colloids was placed in a vacuum drying oven at 60 °C for 12 h to remove remaining water. Finally, nanostructured gelatin films were obtained by peeling them off from the surface of abrasive paper. The as-prepared gelatin films were cut into a size of 5 cm × 5 cm for fabricating the GP-TENG subsequently. The preparation flow chart of the nanostructured gelatin film is shown in Fig. 1(a).

### 2.3. Synthesis of gas-sensing materials

**2.3.1 Synthesis of $NiCo_2O_4$ nanospheres.** The preparation of $NiCo_2O_4$ nanospheres adopted the hydrothermal method and calcination method. First, 40 mmol $NH_4HCO_3$ was dissolved in 80 mL of ethylene glycol. Subsequently, 1 mmol $Ni(CH_3COO)_2 \cdot 4H_2O$ and 2 mmol $Co(CH_3COO)_2 \cdot 4H_2O$ were added to the above solution under the conditions of magnetic stirring. Next, the fully-stirred solution was moved into a 150 mL autoclave and thermally treated at 120 °C for 20 h. The obtained products were repeatedly washed with water and ethanol to remove the impurities adhering to the surface of $NiCo_2O_4$ nanospheres. Pink powders were obtained *via* drying. Finally, the pink powders were calcined at 350 °C for 3 h at a heating speed of 1 °C min$^{-1}$ to get pure black $NiCo_2O_4$ powder.

**2.3.2 Synthesis of PANI nanorods.** First, 0.23 g APS was dissolved in 50 mL deionized water under intense agitation. Thereafter, 2.5 mL HCl and 1 mL aniline were added to the above APS solution. Then, the mixed solution was treated in an ice-water bath (0 °C) for 2 h. Finally, the obtained product was rinsed with deionized water until the pH was close to 3. Black PANI powders were obtained after drying.

**2.3.3 Synthesis of the $PANI/NiCo_2O_4$ composite.** 0.2 g of $NiCo_2O_4$ powders and 0.2 g of PANI powders were dissolved in 10 mL ethanol and stirred for 30 minutes, respectively. $NiCo_2O_4$ solution and PANI solution with a concentration of 20 mg mL$^{-1}$ were obtained through the above step. Then, $NiCo_2O_4$ solution and PANI solution were blended at a mass ratio of 1 : 1, 2 : 1, 1 : 2 and sonicated for 0.5 h to get three solutions with different

**10936** | *J. Mater. Chem. A*, 2022, **10**, 10935–10949

This journal is © The Royal Society of Chemistry 2022

**Fig. 1** (a) The preparation flow chart of the nanostructured gelatin film with abrasive paper as the template. (b) The assembly flow chart of the GP-TENG.

ratios for subsequent experiments to screen out the best doping concentration of $NiCo_2O_4$ and PANI.

## 2.4. Fabrication of the GP-TENG and the GPAS

The GPAS is composed of three parts: one is the GP-TENG, which serves as a constant voltage source to drive the $NH_3$ sensor. Another is the circuit module of rectification and voltage regulation. The other is the $NH_3$ sensor based on the $PANI/NiCo_2O_4$ composite. For the GP-TENG, the gelatin film with a rough surface and the PI film were transferred to the copper foil tape, respectively. The nanostructured gelatin film was used as a positive friction material while the PI film was used as a negative friction material. Copper foil tapes were used as electrodes. The back of copper foil tapes was further pasted with support plates, which could support and protect the copper electrodes and make the force exerted on the surface of friction materials more uniform. The GP-TENG was built by assembling them together, and its effective contact area was $5 \times 5$ cm$^2$. The preparation flow chart of the GP-TENG is shown in Fig. 1(b). A linear reciprocating motor was utilized to simulate external vibrations to drive the GP-TENG to work. For providing stable voltage input for the $NH_3$ sensor, we designed the circuit module of rectification and voltage regulation. The physical picture of the circuit board is

displayed in Fig. S1.† It consisted of an integrated rectifier bridge, a RC filter and two 12 V zener diodes. The GP-TENG was connected with the circuit module of rectification and voltage regulation, which can convert the AC voltage signal output of the GP-TENG into a stable 24 V DC voltage output signal.

The $NH_3$ gas sensor based on the $PANI/NiCo_2O_4$ composite was prepared by a spin-coating technique. Three solutions of PANI : $NiCo_2O_4$ with mass ratios of 1 : 1, 1 : 2, and 2 : 1 as well as 20 mg mL$^{-1}$ solutions of PANI and $NiCo_2O_4$ were coated on Cu/Ni IDEs, respectively. The preparation process of the PANI/$NiCo_2O_4$ composite sensor is exhibited in Fig. 2(a). The experimental test platform of the self-powered GPAS based on the $PANI/NiCo_2O_4$ composite is shown in Fig. 2(b).

## 2.5. Characterization and measurement instruments

A scanning electron microscope (SEM, Hitachi S-4800) was utilized to explore surface morphologies of the nanostructured gelatin film and the $PANI/NiCo_2O_4$ composite. A transmission electron microscope (TEM, Jeoljem-2100) was applied to further study the microstructure of $NiCo_2O_4$ nanospheres. The phase analysis of the gas-sensing materials was carried out by using an X-ray diffractometer (Rigaku D/Max 2500 PC) with Cu Kα radiation. The element composition and chemical binding energy

This journal is © The Royal Society of Chemistry 2022

*J. Mater. Chem. A*, 2022, **10**, 10935–10949 | **10937**

Fig. 2 (a) The diagram of preparation process of the $NH_3$ gas sensor based on the PANI/$NiCo_2O_4$ composite. (b) The experimental test platform of the self-powered GPAS based on the PANI/$NiCo_2O_4$ composite.

of the PANI/$NiCo_2O_4$ composite were analyzed by X-ray photo-electron spectroscopy (XPS, Thermo Scientific K-Alpha XPS spectrometer).

The dry $NH_3$ gas sample used in our experiments was offered by Dalian Date Gas Technology Co., Ltd. The desired concentration could be obtained by diluting the dry $NH_3$ gas sample to a specific volume in a chamber. Various performance parameters of the GPAS were tested at 23% RH and 25 °C *via* using a Keysight 34470A.

## 3. Results and discussion

### 3.1. Characteristics of the nanostructured gelatin film

In this paper, gelatin films with different surface roughness were fabricated using abrasive paper of various meshes as templates. The performance of the GP-TENG was studied through constructing friction pairs between the prepared gelatin films and PI films. It is well recognized that the surface rough-ness of the abrasive paper will increase with the decrease of its meshes. As shown in Fig. S2,† the voltage is low when the untreated gelatin film and the PI film form a friction pair. The

gelatin film fabricated with P1000 abrasive paper as a template shows the best performance for the GP-TENG. The output performance of the GP-TENG is the result of the combined effect of surface charge density and the effective contact area. The surface charge density of the gelatin film prepared with P1000 abrasive paper as a template has saturated. At this time, as the mesh of abrasive paper increases, the effective contact area of the nanostructured gelatin film will decrease, which will lead to a decrease in the output voltage of the GP-TENG. Therefore, nanostructured gelatin films applied in subsequent experiments were all prepared with P1000 abrasive paper. Fig. S3† shows the SEM images of the nanostructured gelatin film prepared with P1000 abrasive paper. It can be clearly seen that numerous concave microstructures on the surface of the gelatin film because of peeling it off from the surface of the abrasive paper. Most of microstructures deform or collapse due to the soft nature of the gelatin polymer, and the size of the microholes is between 10 μm and 15 μm. Nanostructured gelatin films increase the effective contact area, which can induce more charges through

10938 | *J. Mater. Chem. A*, 2022, 10, 10935–10949

This journal is © The Royal Society of Chemistry 2022

contact-electrification. Gelatin films also exhibit brilliant degradability. Water degradation experiments demonstrate that gelatin films could be easily degraded in water, particularly in hot water. The degradation process of gelatin films in cold water and hot water is shown in Fig. S4.†

### 3.2. Working principle of the GP-TENG

The operation pattern of the GP-TENG is typical contact-separation. The working principle of the GP-TENG is

illustrated in Fig. 3(a). When the nanostructured gelatin film and the PI film are in complete contact for the first time under the action of external force, positive charges and negative charges accumulate on the surface of the nanostructured gelatin film and the PI film due to different electron affinities of the friction materials, respectively; (i) once the two friction layers are separated, a potential difference is generated between the two friction layers due to electrostatic induction, which will drive electrons to flow from the bottom electrode to the top
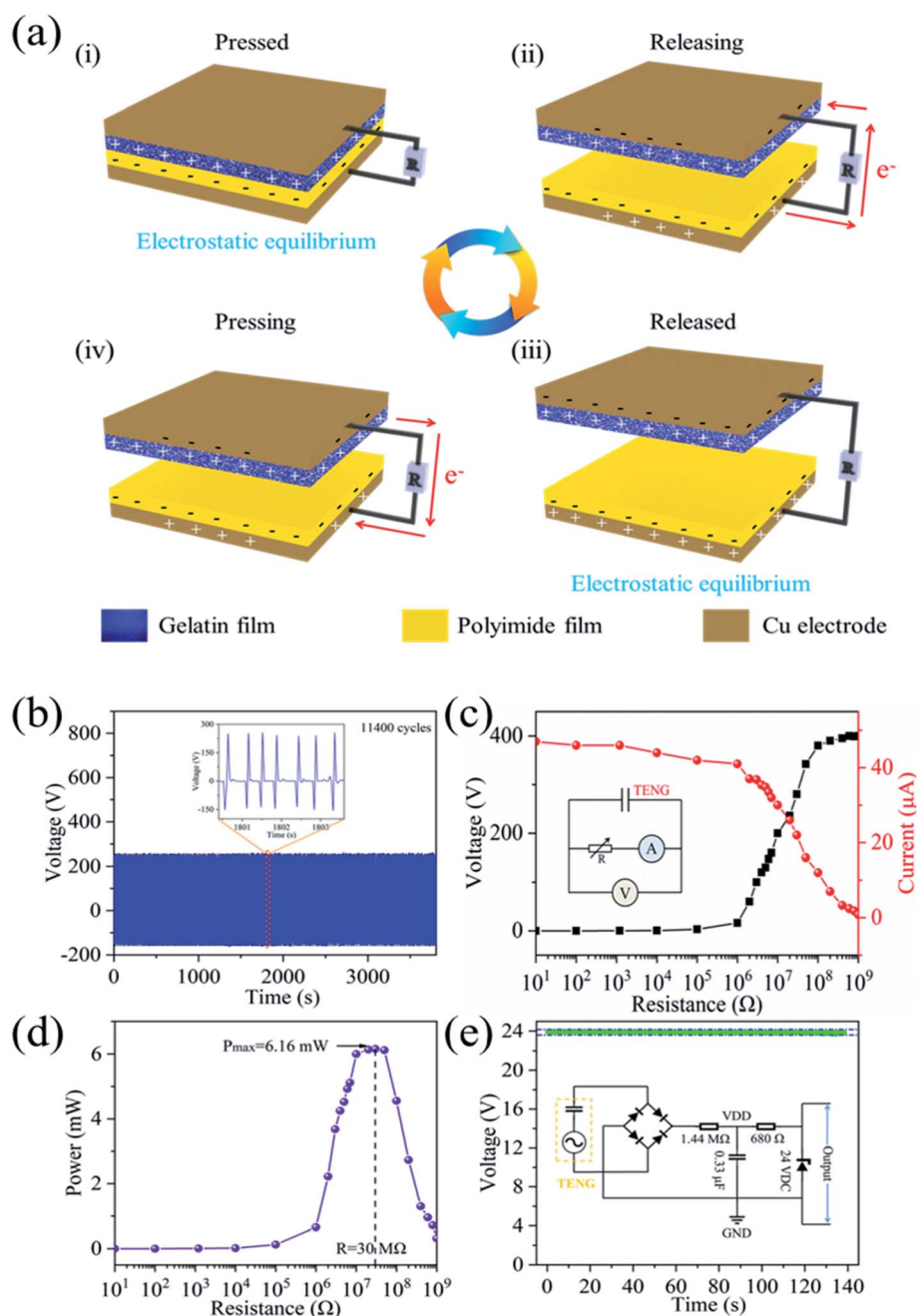


Fig. 3 (a) Working principle of the GP-TENG. (b) The mechanical stability of the GP-TENG (3 Hz). Inset: partially enlarged signal view of the GP-TENG. (c) Variation trends of the open-circuit voltage ($V_{oc}$) and short-circuit current ($I_{sc}$) of the GP-TENG when the load resistance changes from 0 Ω to 1 GΩ. Inset: the equivalent measurement circuit diagram. (d) Plot of the power *versus* the loading resistance. (e) The steady output voltage of the GP-TENG with a rectification and voltage regulation circuit module. Inset: the signal processing circuit for the GP-TENG.

This journal is © The Royal Society of Chemistry 2022

*J. Mater. Chem. A*, 2022, **10**, 10935–10949 | **10939**

electrode through the load resistance; (ii) subsequently, electrostatic equilibrium is reached, and no current flows in the external circuit at this time; (iii) when the two friction layers contact again, an opposite potential difference is generated, which causes electrons to flow in the reverse direction; (iv) charges are transferred back and forth in the external circuit by continuous contact and separation.[33] Therefore, voltage signals and current signals are alternately generated.

### 3.3. Output performance measurement of the GP-TENG

The output performance of the GP-TENG was first optimized by adjusting the initial separation distance, area, force and vibration frequency. Fig. S5(a)† shows the output performance of the GP-TENG for different initial separation distances at 3 Hz and a force of 20 N. When the separation distance increases from 2 mm to 6 mm, both $V_{oc}$ and $I_{sc}$ increase, which is attributed to the increase in the charge transfer speed between the two friction layers. A further increase in the separation distance will weaken the electrostatic induction between the two friction layers, leading to a decrease in output performance of the GP-TENG. Therefore, the separation distance between the two friction layers was set to 6 mm in the subsequent experiments. Fig. S5(b)† shows the output performance of the GP-TENG of different sizes at 3 Hz and a force of 20 N. The GP-TENG with an area of $5 \times 5$ cm$^2$ holds the best output performance. The larger area of the friction layers will increase the charge accumulation, and the flow of charges during the operation of the GP-TENG will lead to the increase of $V_{oc}$ and $I_{sc}$. The influence of forces on the output performance of the GP-TENG is shown in Fig. S5(c);† both $V_{oc}$ and $I_{sc}$ increase when the force increases from 2 N to 15 N, which is due to the increase in the effective contact area of the GP-TENG. When a force of 20 N is applied, $V_{oc}$ and $I_{sc}$ do not increase significantly because the effective contact area has been maximized. The influence of the vibration frequency on the output performance of the GP-TENG is shown in Fig. S5(d).† As the frequency increases from 1 Hz to 5 Hz, $V_{oc}$ remains unchanged while $I_{sc}$ increases. At different vibration frequencies, the total charge of the external circuit remains unchanged, so $V_{oc}$ is stable. The charge transfer speed becomes faster at high frequencies, which leads to an increase in $I_{sc}$.

The output performance of the GP-TENG at different temperatures and humidities was investigated at 20 N, 3 Hz and a separation distance of 6 mm. Fig. S6(a)† shows the cycling stability of the GP-TENG at different relative humidities and 25 °C. The relative humidity has a great influence on the GP-TENG. With the increase of the relative humidity, the output voltage of the GP-TENG decreases significantly. Fig. S6(b)† shows the cycling stability of the GP-TENG at different temperatures and 23% RH. The $V_{oc}$ change of the GP-TNEG is not very obvious when the temperature varies from 10 °C to 30 °C.

Long-term stability of the GP-TENG was tested at a vibration frequency of 3 Hz. As elucidated in Fig. 3(b), the peak-to-peak value of the GP-TENG could reach 400 V and remains constant even after 11 400 cycles, which demonstrates that the GP-TENG holds remarkable mechanical stability. The inset

**Table 1** Performance comparison of different gelatin-based TENGs

| Triboelectric materials | $V_{oc}$ (V) | Power density (mW m$^{-2}$) | Ref. |
| --- | --- | --- | --- |
| Fish gelatin and fish gelatin | 500 | 1000 | 25 |
| Gelatin and PTFE/PDMS | 130 | 458 | 26 |
| Gelatin/glycerol and PTFE | 58.2 | 116 | 34 |
| Gelatin and polyimide | 400 | 2464 | This work |

partially captures the voltage signal of the GP-TENG. As the external load resistance varies from 10 Ω to 1 GΩ, variation trends of the open circuit voltage ($V_{oc}$) and short circuit current ($I_{sc}$) of the GP-TENG are elucidated in Fig. 3(c). The inset depicts the equivalent circuit diagram. According to Ohm's law, the $V_{oc}$ keeps increasing while the $I_{sc}$ keeps reducing as the load resistance increases. The relationship curve between power and load resistance is exhibited in Fig. 3(d). When external load resistance increases, the power first increases and then decreases. When external load resistance reaches 30 MΩ, the output power could reach 6.16 mW, which is sufficient to drive low-powered electronic devices, such as calculators, LEDs and gas sensors, to operate normally. As illustrated in Fig. 3(e), the AC voltage signal output of the GP-TENG is converted into a 24 V DC voltage signal after being processed by the circuit module of rectification and voltage regulation. The inset depicts the test circuit. It can be seen that the 24 V DC voltage signal is stable. The performance of the GP-TENG is compared with that of other gelatin-based TENGs in Table 1. The GP-TENG has excellent output performance by comparison.[25,26,34]

### 3.4. Multifunctional applications of the GP-TENG

The GP-TENG possesses great application potential and can power microelectronic devices and monitor signals of human motions. First, the GP-TENG was used as a micro-nano energy source to power electronic devices. As shown in Fig. 4(a), 82 blue LEDs connected in series in a "gelatin" pattern could be directly driven by the GP-TENG (Video 1†). The charging capability of the GP-TENG was assessed through charging 0.22 µF, 0.33 µF and 1 µF capacitors, respectively. As illustrated in Fig. 4(b), the charging time of the GP-TENG got shorter as the capacitance decreased. Since AC signals generated by the GP-TENG cannot directly supply power to DC devices such as calculators, AC signals output by the GP-TENG were converted into DC signals to drive a digital calculator. Fig. 4(c) indicates that the digital calculator could run normally under continuous contact-separation of the GP-TENG. The circuit schematic for driving low-powered micro electronic devices is depicted in Fig. 4(d).

Secondly, it could be used as a self-powered motion sensor. The GP-TENG could generate distinct electrical signals from various human motions without an extra power source. Fig. 4(e) shows the schematic diagram of the structure of the GP-TENG for body motion detection. The inset shows the physical image of the GP-TENG used for body motion detection. The nanostructured gelatin film and the PI film were cut into a size of 5 cm × 5 cm, respectively. Copper foil tapes were glued to their back as electrode layers. Printing paper adhered to the
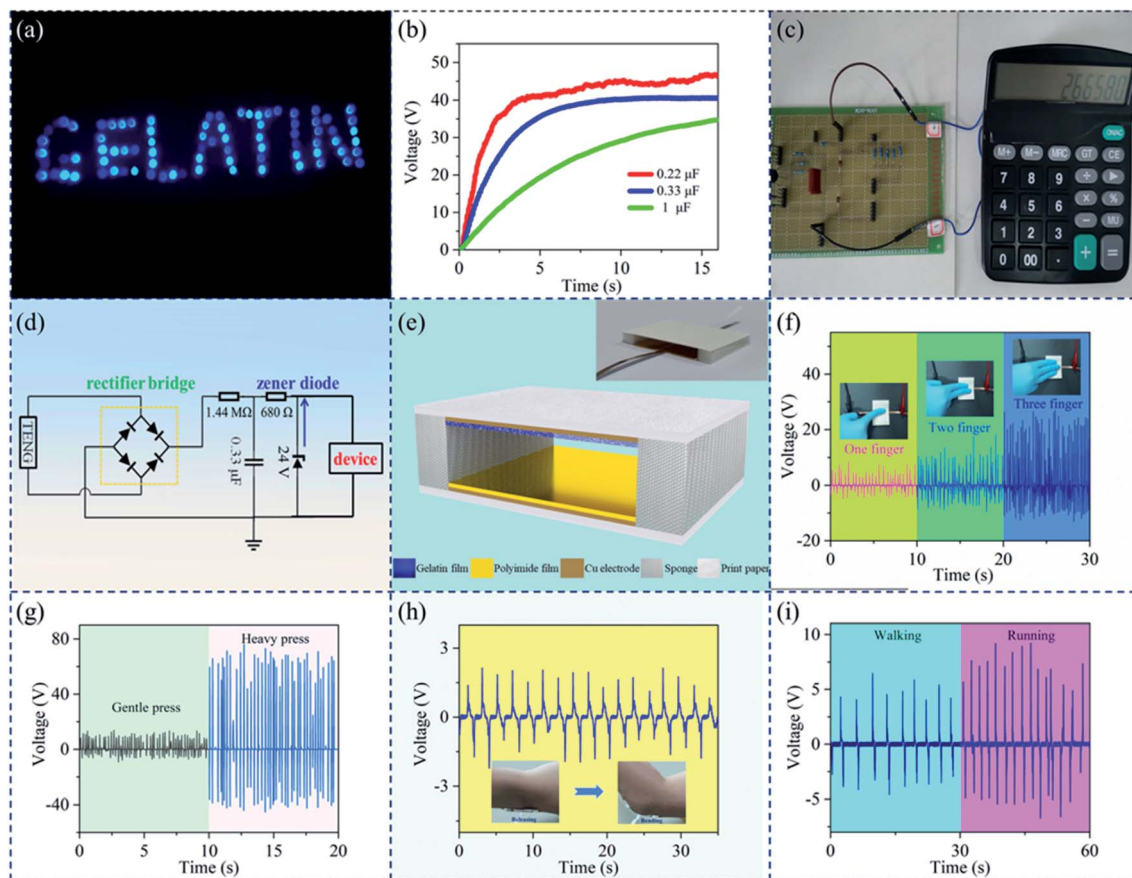
**Fig. 4** (a) Blue LEDs connected in series in a "gelatin" pattern could be driven by the GP-TENG. (b) Variation curves in the voltage of different capacitors. (c) The digital calculator could run normally under continuous contact-separation of the GP-TENG. (d) The circuit schematic for driving low-powered micro electronic devices (e) the schematic diagram of the structure of the GP-TENG for body motion detection. The inset: the physical image of the GP-TENG used for body motion detection. (f) Output voltage of the GP-TENG upon tapping with different numbers of fingers. (g) Output voltage of the GP-TENG upon tapping with different forces. (h) Output voltage of the GP-TENG during repeated bending and releasing of an arm. (i) Two different sport states of running and walking recognized by the GP-TENG in real time.

backside of electrode layers as substrates. Two pieces of mela-mine sponges (thickness of 6 mm) were used as spacers to separate the two friction layers. Electricity was generated through contact and separation of the two friction layers driven by various human body motions. The GP-TENG can consecu-tively sense the number of fingers pressed on it. As shown in Fig. 4(f), the voltage increases as the number of fingers increases. This is because the increase in the number of fingers will not only increase the contact area of the two friction layers of the GP-TENG, but also increase the force exerted on the two friction layers. Enhancement of output voltage results from both of the two factors. As exhibited in Fig. 4(g), the magnitude of the force applied on the GP-TENG could also be monitored. Output voltage of the GP-TENG varies significantly under two different magnitudes of gentle press and heavy press. The GP-TENG could also detect other body motion signals. As eluci-dated in Fig. 4(h), the GP-TENG was attached to the human elbow joint. Regular voltage signals were produced after repeated releasing and bending of the elbow joint (Video 2†). The GP-TENG installed on the sole could recognize two different sport states of running and walking in real time (Fig. 4(i)).

### 3.5. Characterization of gas-sensing materials

Fig. 5(a) and (b) show the SEM images of the prepared $NiCo_2O_4$ at different scales. The prepared $NiCo_2O_4$ has a solid nano-sphere structure and a smooth surface. Fig. 5(c) and (d) present the SEM images of the $PANI/NiCo_2O_4$ composite. It could be clearly seen that nanorod-shaped PANI firmly adhered to the $NiCo_2O_4$ nanospheres, which could improve adsorption ability for the target gas. TEM and HRTEM were utilized to observe microstructures of $NiCo_2O_4$ nanospheres. Fig. 5(e) and (f) show the TEM images of $NiCo_2O_4$ nanospheres at different magnifi-cations. The high-resolution TEM (HRTEM) image is shown in Fig. 5(g); neatly arranged lattice fringes are observed, and a lattice spacing of 0.47 nm corresponds to the (111) plane of the $NiCo_2O_4$ crystal.[35] Fig. 5(h) illustrates that the SAED pattern of $NiCo_2O_4$ holds an obvious ring structure. The (440), (511), (400), (311) and (220) planes accord with the crystal plane of $NiCo_2O_4$, which indicates that the prepared $NiCo_2O_4$ possesses a polycrystalline structure.[36]

The XRD patterns of pure PANI, pure $NiCo_2O_4$ and the $PANI/NiCo_2O_4$ composite are exhibited together in Fig. 6(a). The three samples were scanned within a diffraction angle of 10°–80°. The
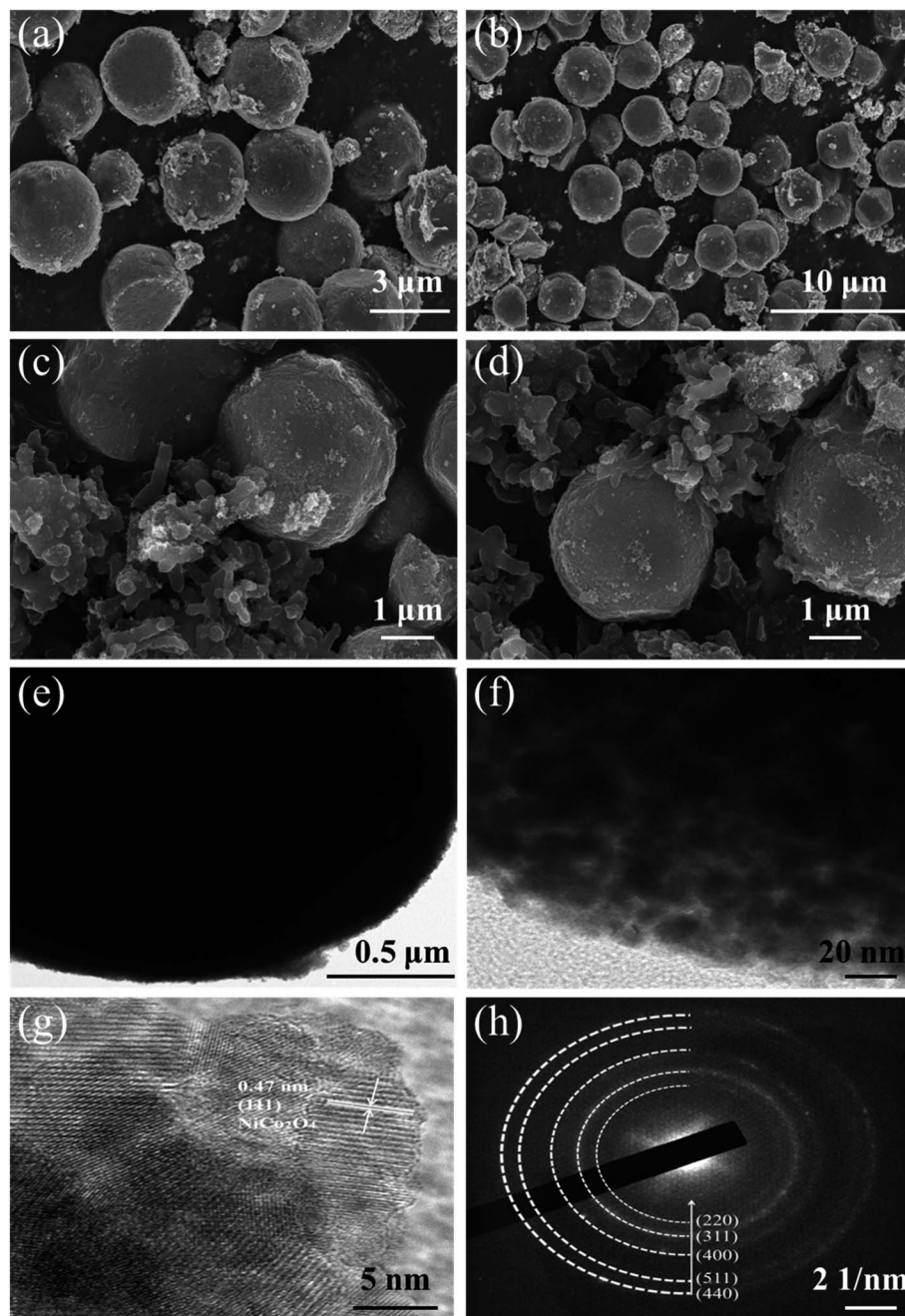
Fig. 5 SEM images of (a and b) $NiCo_2O_4$ nanospheres at different scales. (c and d) The PANI/$NiCo_2O_4$ composite. TEM images of (e and f) $NiCo_2O_4$ nanospheres at different magnifications. (g) HRTEM images of $NiCo_2O_4$ nanospheres. (h) The corresponding SAED pattern of $NiCo_2O_4$ nanospheres.

three main characteristic peaks of PANI are located at 2θ of 14.8°, 20.4° and 25.5°, which correspond to (011), (020) and (200) planes of PANI.[37] The above three peaks observed are due to the parallel and vertical periodicity of PANI chains.[38] These peaks indicate that PANI holds extremely low crystallinity due to the repetition of benzene and quinone rings on PANI chains.[39] The dominant characteristic peaks of $NiCo_2O_4$ nanospheres are located at 18.9°, 31.3°, 36.8°, 38.4°, 44.7°, 55.5°, 59.5° and 65.2°, corresponding to planes of (111), (220), (311), (222), (400), (422), (511) and (440) (JCPDS No. 073-1702).[40] In the XRD pattern of

the PANI/$NiCo_2O_4$ composite, all main characteristic peaks of pure PANI and pure $NiCo_2O_4$ could be observed, and no other conspicuous peaks are observed, which indicates that doped composite materials are of high purity.

The XPS survey spectrum of the PANI/$NiCo_2O_4$ composite is shown in Fig. 6(b). The existence of Ni, Co, O, N and C has been confirmed. In the Ni 2p spectrum of the PANI/$NiCo_2O_4$ composite, two pairs of spin–orbit doublets at 854.93/872.81 eV and 853.51/870.58 eV are observed, which correspond to $Ni^{3+}$ and $Ni^{2+}$, and two shakeup satellite peaks of Ni are located at
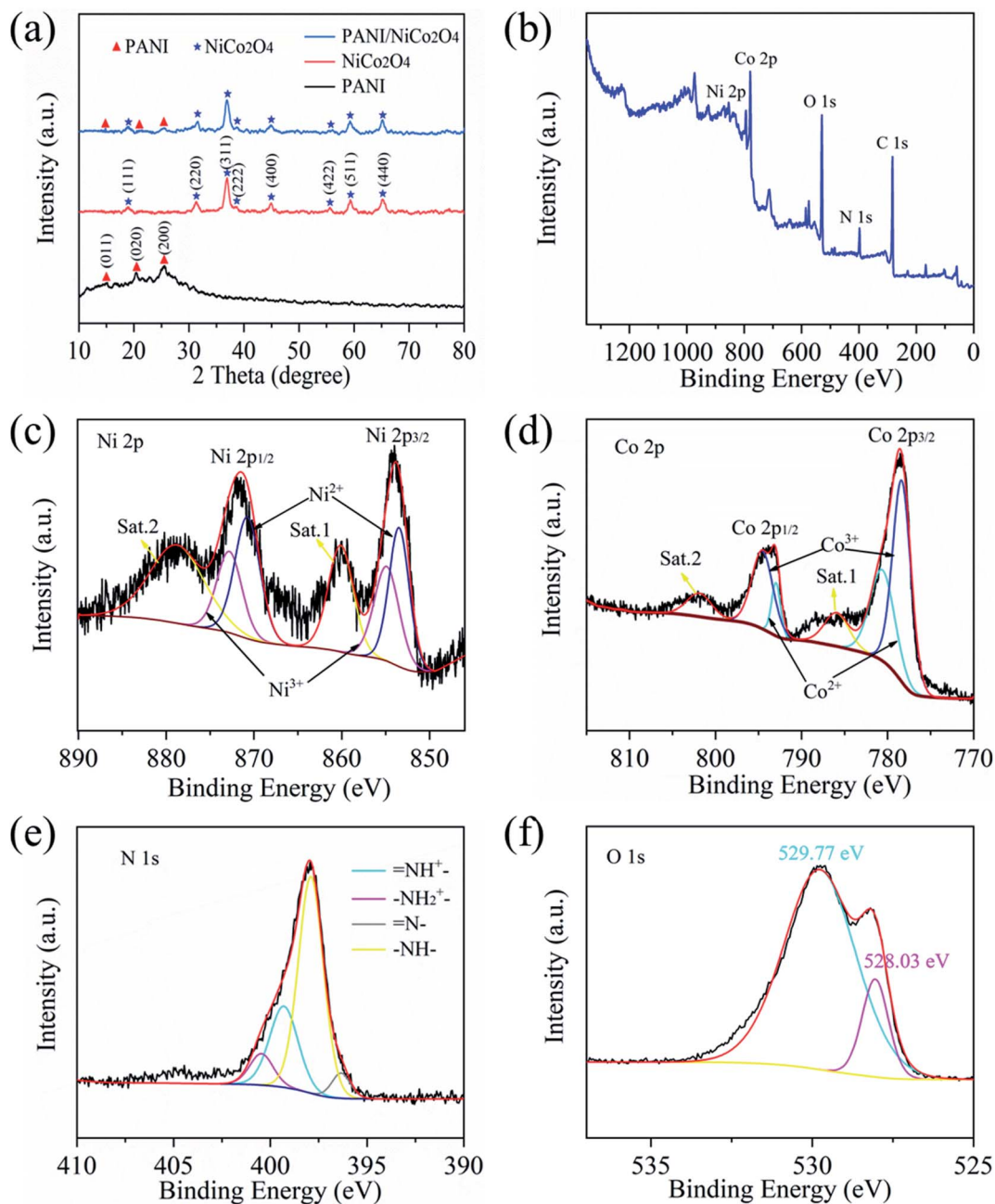
Fig. 6 (a) XRD pattern of pure PANI, pure NiCo$_2$O$_4$ and the PANI/NiCo$_2$O$_4$ composite. XPS spectra of the PANI/NiCo$_2$O$_4$ composite: the (b) survey spectrum, (c) Ni 2p spectrum, (d) Co 2p spectrum, (e) N 1s spectrum and (f) O 1s spectrum.

860.07 eV and 878.90 eV (Fig. 6(c)).[41] Similarity, the XPS spectrum of Co 2p shows the binding energies of Co 2p$_{1/2}$, Co 2p$_{3/2}$ and two shakeup satellites. Two fitted peaks of 793.82 eV and 780.60 eV correspond to Co$^{2+}$, while fitted peaks at 778.90 eV and 795.0 eV correspond to Co$^{3+}$ (Fig. 6(d)).[42] The XPS spectrum of N 1s is exhibited in Fig. 6(e); two main peaks of 397.90 eV and 399.34 eV are attributed to groups of –NH– and =NH$^+$–, respectively. The two lower peaks of 396.36 eV and 400.45 eV are due to the =N– and –NH$_2$$^+$– groups, respectively.[43] The above results of the N 1s spectrum indicate the successful synthesis of PANI. The XPS spectrum of O 1s is shown in Fig. 6(f). Two peaks

with binding energies of 528.03 eV and 529.77 eV are contributed by the lattice oxide oxygen of Ni–O and Co–O.[44]

### 3.6. NH$_3$-sensing properties of the GPAS

A self-powered GPAS is constructed by integrating the GP-TENG, the circuit module of rectification and voltage regulation and the PANI/NiCo$_2$O$_4$ ammonia sensor. NH$_3$-sensing performance of the GPAS has been systematically studied. The voltage response of the GPAS is defined as $R = V_g/V_a$, where $V_g$ and $V_a$ are the output voltage values of the GPAS when exposed to a certain concentration of NH$_3$ and air, respectively. First, we determined

the appropriate mass ratio of PANI and $NiCo_2O_4$ to ensure the best response of the $NH_3$ sensor. The resistance change of the five samples with different mass ratios at an $NH_3$ concentration of 0–20 ppm is exhibited in Fig. 7(a). The change of response ($R_g/R_a$) is shown in Fig. 7(b). Pure $NiCo_2O_4$ nanospheres hold a very low response towards $NH_3$ while PANI nanorods are extremely sensitive towards $NH_3$. Doping $NiCo_2O_4$ and PANI can further improve the response of the sensor. When the mass ratio of PANI and $NiCo_2O_4$ is 2 : 1, the resistance response of the $NH_3$ sensor is significantly higher than that of the other samples. The $NH_3$ sensors used in the subsequent experimental process were prepared according to this mass ratio. The change curve of the capacitor in the signal processing circuit after three cycles of charging and discharging is shown in Fig. 7(c). Due to the presence of two 12 V zener diodes at the rear of the signal processing circuit, the voltage saturation value is limited to 24 V. When the GP-TENG starts to run, a stable 24 V voltage signal can be rapidly reached in about 12 s. In order to make the GPAS have better sensitivity, a 5 MΩ resistor is connected in series with the gas sensor based on the principle of voltage division, which can better realize the differentiation of different $NH_3$ concentrations. Fig. 7(d) exhibits the voltage change curve of the GPAS at six different $NH_3$ concentrations. The output voltage of the GPAS is proportional to the $NH_3$ concentration. The inset shows the fitting curve between the $NH_3$ concentration and voltage response. It can be seen that the GPAS possesses great linearity ($R^2 = 0.9767$) and excellent sensitivity (0.166). Fig. 7(e) and (f) display response/recovery output voltage curves at $NH_3$ concentrations of 1 ppm and 10 ppm, respectively. The response/recovery time is 39 s/54 s at an $NH_3$ concentration of 1 ppm and 25 s/59 s at an $NH_3$ concentration of 10 ppm, which indicates that the GPAS has relatively fast performance of response and recovery. Fig. 7(g) demonstrates the repeatability characteristic of the GPAS at $NH_3$ concentrations of 1 ppm and 3 ppm, respectively. The voltage of the GPAS can still return to the original state after three cycles of gas injection and exhaust, which shows that the GPAS has awesome repeatability. The selectivity test result of the GPAS is shown in
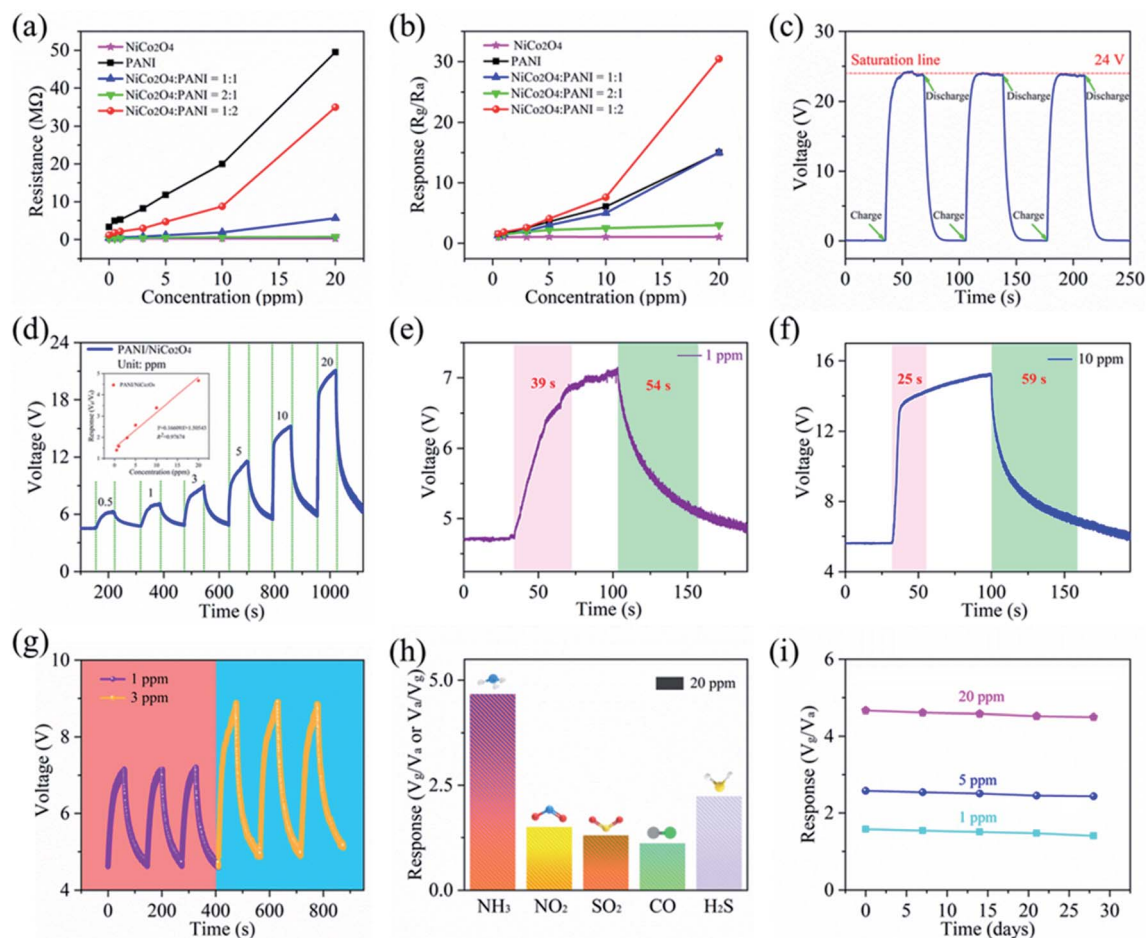


Fig. 7 (a and b) The resistance change and response ($R_g/R_a$) change of the five samples with different mass ratios at an $NH_3$ concentration of 0–20 ppm. (c) The change curve of the capacitor in the signal processing circuit after three cycles of charging and discharging. (d) The voltage change curve of the GPAS at six different $NH_3$ concentrations of 500 ppb, 1 ppm, 3 ppm, 5 ppm, 10 ppm and 20 ppm. (e and f) The response/recovery output voltage curve at $NH_3$ concentrations of 1 ppm and 10 ppm, respectively. (g) The repeatability characteristic of the GPAS at $NH_3$ concentrations of 1 ppm and 3 ppm. (h) The selectivity test result of the GPAS. (i) Long-term stability of the GPAS at various $NH_3$ concentrations in one month.

**Table 2** NH$_3$ sensing properties of the GPAS based on the PANI/NiCo$_2$O$_4$ composite in this work compared with those of previous studies

| Sensor materials | Signal type | Response/recovery time | Response | Ref. |
|---|---|---|---|---|
| PANI/MWCNTs | Self-powered voltage | 120 s/137 s | 2.55 (100 ppm) | 19 |
| PANI/Nb$_2$CT$_x$ | Self-powered voltage | 105 s/143 s | 3 (100 ppm) | 20 |
| C-PANI NFs | Self-powered voltage | 40 s/255 s | 1.25 (500 ppm) | 45 |
| Ce-doped ZnO/PANI | Self-powered voltage | 109 s/233 s | 1.75 (25 ppm) | 46 |
| PANI/NiCo$_2$O$_4$ | Self-powered voltage | 22 s/62 s | 4.67 (20 ppm) | This work |

Fig. 7(h). The voltage response of the GPAS towards five different gases (NH$_3$, NO$_2$, SO$_2$, CO, and H$_2$S) was studied at a concentration of 20 ppm. It can be seen that the GPAS exhibits the highest selectivity towards NH$_3$. The response of the GPAS was tested at three NH$_3$ concentrations of 1 ppm, 5 ppm and 20 ppm every seven days within a month. Fig. 7(i) shows variation trends of the GPAS response in one month. The response value of the GPAS within one month only slightly decreases, which indicates that the GPAS holds excellent long-term stability. The detection limit is calculated to be 216 ppb based on a signal to noise ratio of $3(\sigma/S)$. Fig. S7(a)† shows the response ($R_g/R_a$) of the PANI/NiCo$_2$O$_4$ gas sensor towards 10 ppm NH$_3$ in different humidity environments (23–67% RH). The change of RH has an influence on the sensor response toward NH$_3$ sensing. Fig. S7(b)† shows the response ($V_g/V_a$) of the GPAS under 23–67% RH. The effect of humidity on the GPAS is significantly reduced. The comparison results between this work and previously reported NH$_3$ sensors are summarized in Table 2. The GPAS exhibits quite excellent advantages for detecting NH$_3$ gas.[19,20,45,46]

### 3.7. NH$_3$-sensing mechanism

The gas-sensing mechanism of semiconductor gas sensors is related to the resistance changes of gas-sensing materials exposed to different concentrations of target gases.[47] This process follows the charge transfer model. The increase or decrease of the sensor resistance depends on the oxidation/reduction characteristics of the target gas and the majority carrier type (electrons/holes) of the gas-sensing material.[48] Both NiCo$_2$O$_4$ and PANI are p-type semiconductors, where holes are majority carriers.[39,49] The gas adsorption and desorption processes occur on the surface of NiCo$_2$O$_4$ nanospheres. Fig. 8(a) and (b) vividly depict the gas adsorption and desorption processes on the surface of NiCo$_2$O$_4$ nanospheres in air and NH$_3$, respectively. In air, O$_2$ is chemically adsorbed on the surface of NiCo$_2$O$_4$ nanospheres and converted into O$_2^-$ by extracting free electrons from the conduction band of NiCo$_2$O$_4$ nanospheres.[50] When the sensor is placed in NH$_3$, NH$_3$ molecules will be oxidized by O$_2^-$ and the trapped electrons will be released to the surface of NiCo$_2$O$_4$ nanospheres.[51] The concentration of holes will be reduced because these released electrons will combine with holes.

In the PANI/NiCo$_2$O$_4$ composite, PANI plays a dominant role in the response towards NH$_3$ gas. The mechanism of PANI towards NH$_3$ is related to protonation/deprotonation (Fig. S8†). In NH$_3$, protons in the acidified PANI are captured by NH$_3$. This process causes PANI to change from a conductive emeraldine salt (ES) state

to a non-conductive emeraldine base (EB) state, which will increase resistance of the pure PANI sensor.[52] Resistance of the pure PANI sensor will decrease because this process is reversible in air. Compared with pure PANI, doping PANI and NiCo$_2$O$_4$ greatly improves the response of sensors towards NH$_3$. This phenomenon can be explained by three factors: the unique morphological structure formed by doping PANI and NiCo$_2$O$_4$; formation of a p–p heterojunction; the "electrical catalytic" effect of NiCo$_2$O$_4$.

First, regulation morphologies of nanomaterials can effectively boost the diffusion of oxygen molecules/target gases on the surface of gas-sensing materials.[53] Numerous nanorod-shaped PANI spread on the smooth surface of NiCo$_2$O$_4$ nanospheres can provide more surface active sites and a larger specific surface area, which promotes adsorption ability of the target gas. Secondly, a heterojunction will be generated at the contact interface when different semiconductor materials are in contact with each other, which can regulate resistance of the sensitive materials to improve the sensing performance.[54] The energy band structure diagram before contact of PANI and NiCo$_2$O$_4$ is exhibited in Fig. 8(c); the energy band gap of PANI and NiCo$_2$O$_4$ is 2.8 eV and 2.6 eV, respectively.[55,56] When two materials are in contact with each other, electrons will transfer from PANI to NiCo$_2$O$_4$ while holes will flow in the reverse direction since the Fermi level of PANI is higher than that of NiCo$_2$O$_4$. This could cause the formation of a hole depletion layer (HDL) on the NiCo$_2$O$_4$ side while a hole accumulation layer (HAL) on the PANI side (Fig. 8(d)). A potential barrier will be constructed at the interface of PANI and NiCo$_2$O$_4$. At the same time, the energy band will be bent in order to balance the Fermi level, which will result in the creation of an extra potential barrier ($q\Delta E_s$).[57] In air, some holes will be generated in the process of oxygen molecules being converted into chemically adsorbed oxygen anions. These holes will be transferred to the hole depletion layer (HDL) due to the difference in the hole concentration, which will make the HDL narrow and then result in a reduction in the height of the potential barrier (Fig. 8(e)). The reaction of NH$_3$ molecules with chemically adsorbed oxygen anions will release trapped electrons back to the surface of gas-sensing materials. The combination of released electrons and holes will widen the HDL layer and increase the barrier height (Fig. 8(f)). The relationship between the resistance value of the semiconductor sensor and the barrier height of the heterojunction could be represented by the following formula:[58]

$$R = R_0 \exp(qE/kT) \qquad (1)$$

where $R$ is the resistance of the sensor, and $R_0$ is the initial resistance of the sensor. $E$ and $q$ are the barrier height of the
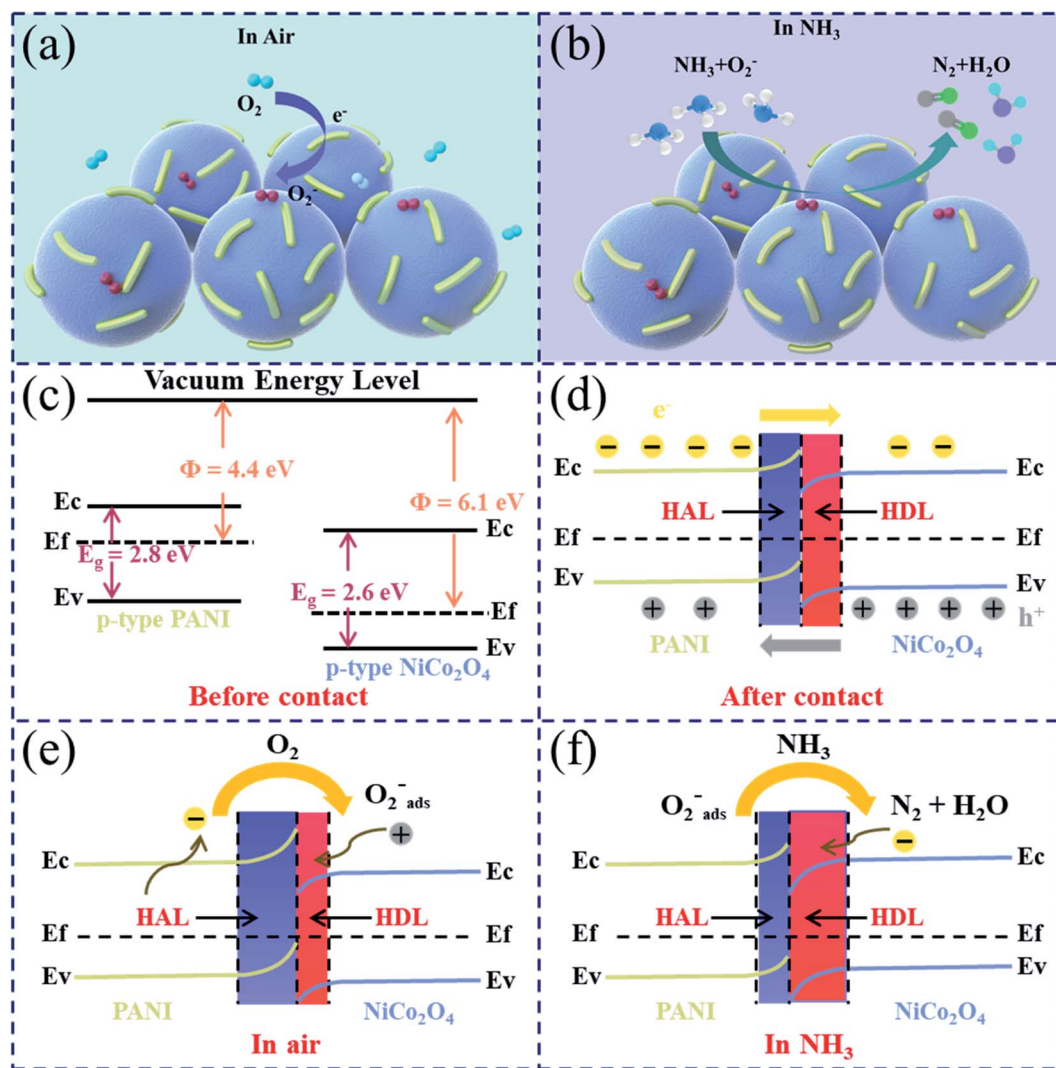
This journal is © The Royal Society of Chemistry 2022

*J. Mater. Chem. A*, 2022, **10**, 10935–10949 | **10945**

Fig. 8 (a and b) Gas adsorption and desorption processes on the surface of $NiCo_2O_4$ nanospheres in air and $NH_3$, respectively. (c and d) The energy band diagram of PANI and $NiCo_2O_4$ before and after contact, respectively. (e and f) The energy band structure of the PANI/$NiCo_2O_4$ heterojunction exposed to air and $NH_3$, respectively.

heterojunction and the electron charge, respectively. $K$ and $T$ are Boltzmann's constant and absolute temperature, respectively. It can be seen from eqn (1) that resistance of the sensor has an exponential relationship with the heterojunction barrier height, which means that even a small variation in $E$ will cause a drastic change in the resistance of the sensor.[59] The p–p heterojunction serves as a hole pump to regulate the resistance of the sensor which is a crucial factor to enhancing the response of chemoresistive gas sensors.[60] Finally, the highly oxidized redox pair $Ni^{3+}/Ni^{2+}$ and $Co^{3+}/Co^{2+}$ present in $NiCo_2O_4$ will be more conducive to the adsorption of $O_2$.[56] The "electrical catalytic" effect enables $NiCo_2O_4$ to absorb more $NH_3$, which will result in better performance.

## 4. Conclusion

To sum up, a high-performance $NH_3$ sensor based on the PANI nanorod/$NiCo_2O_4$ nanosphere composite driven by a degradable, eco-friendly gelatin-polyimide based triboelectric nanogenerator (GP-TENG) was demonstrated. The GP-TENG could generate stable voltage output through the contact-separation of the nanostructured gelatin film and the polyimide film, which could drive LEDs and digital calculators and also could sense physiological signals. The PANI nanorod/$NiCo_2O_4$ nanosphere composite was coated on IDEs through a spin-coating technique to establish the $NH_3$ sensor. In order to provide stable voltage input signals to the gas sensor, a rectification and voltage regulation circuit module was designed. The GPAS shows excellent response and rapid response/recovery time towards $NH_3$. It also possesses great repeatability and long-term stability. In addition, the GPAS holds excellent selectivity towards $NH_3$. The enhanced performance of gas-sensing is attributed to the unique nanostructure formed by doping PANI nanorods and $NiCo_2O_4$ nanospheres, the formation of the p–p heterojunction, and the "electrical catalytic" effect of $NiCo_2O_4$ nanospheres. This study also

10946 | J. Mater. Chem. A, 2022, 10, 10935–10949

This journal is © The Royal Society of Chemistry 2022

provides novel ideas for the design of wearable gas sensors and human motion sensors.

## Conflicts of interest

The authors declare that they have no conflict of interest.

## Acknowledgements

## References

1 D. W. Lv, W. F. Shen, W. G. Chen, R. Q. Tan, L. Xu and W. J. Song, PSS-PANI/PVDF composite based flexible $NH_3$ sensors with sub-ppm detection at room temperature, *Sens. Actuators, B*, 2021, **328**, 129085.

2 Q. N. Pan, T. T. Li and D. Z. Zhang, Ammonia gas sensing properties and density functional theory investigation of coral-like Au-SnSe$_2$ Schottky junction, *Sens. Actuators, B*, 2021, **332**, 129440.

3 A. F. Smith, X. M. Liu, T. L. Woodard, T. D. Fu, T. Emrick, J. M. Jimenez, D. R. Lovley and J. Yao, Bioelectronic protein nanowire sensors for ammonia detection, *Nano Res.*, 2020, **13**, 1479–1484.

4 D. Y. Wang, D. Z. Zhang, Y. Yang, Q. Mi, J. H. Zhang and L. D. Yu, Multifunctional latex/polytetrafluoroethylene-based triboelectric nanogenerator for self-powered organ-like MXene/metal-organic framework-derived CuO nanohybrid ammonia sensor, *ACS Nano*, 2021, **15**, 2911–2919.

5 R. T. Huang, H. Wu and L. J. Yang, Study on the ammonia emission characteristics in an ammonia-based WFGD system, *Chem. Eng. J.*, 2020, **379**, 122257.

6 X. W. Wang, D. Z. Zhang, H. B. Zhang, L. K. Gong, Y. Yang, W. H. Zhao, S. J. Yu, Y. D. Yin and D. F. Sun, In situ polymerized polyaniline/MXene (V$_2$C) as building blocks of supercapacitor and ammonia sensor self-powered by electromagnetic-triboelectric hybrid generator, *Nano Energy*, 2021, **88**, 106242.

7 D. Z. Zhang, Z. M. Yang, P. Li, M. S. Pang and Q. Z. Xue, Flexible self-powered high-performance ammonia sensor based on Au-decorated MoSe$_2$ nanoflowers driven by single layer MoS$_2$-flake piezoelectric nanogenerator, *Nano Energy*, 2019, **65**, 103974.

8 Y. J. Su, G. R. Chen, C. X. Chen, Q. C. Gong, G. Z. Xie, M. L. Yao, H. L. Tai, Y. D. Jiang and J. Chen, Self-powered respiration monitoring enabled by a triboelectric nanogenerator, *Adv. Mater.*, 2021, **33**, 2101262.

9 D. Z. Zhang, D. Y. Wang, Z. Y. Xu, X. X. Zhang, Y. Yang, J. Y. Guo, B. Zhang and W. H. Zhao, Diversiform sensors and sensing systems driven by triboelectric and piezoelectric nanogenerators, *Coord. Chem. Rev.*, 2021, **427**, 213597.

10 W. H. Xu, H. X. Zheng, Y. Liu, X. F. Zhou, C. Zhang, Y. X. Song, X. Deng, M. Leung, Z. B. Yang, R. X. Xu, Z. L. Wang, X. C. Zeng and Z. K. Wang, A droplet-based electricity generator with high instantaneous power density, *Nature*, 2020, **578**, 392.

11 H. Ryu, H. M. Park, M. K. Kim, B. Kim, H. S. Myoung, T. Y. Kim, H. J. Yoon, S. S. Kwak, J. Kim, T. H. Hwang, E. K. Choi and S. W. Kim, Self-rechargeable cardiac pacemaker system with triboelectric nanogenerators, *Nat. Commun.*, 2021, **12**, 4374.

12 C. Y. Li, D. Liu, C. Q. Xu, Z. M. Wang, S. Shu, Z. R. Sun, W. Tang and Z. L. Wang, Sensing of joint and spinal bending or stretching *via* a retractable and wearable badge reel, *Nat. Commun.*, 2021, **12**, 2950.

13 X. Yin, D. Liu, L. L. Zhou, X. Y. Li, G. Q. Xu, L. Liu, S. X. Li, C. G. Zhang, J. Wang and Z. L. Wang, A motion vector sensor *via* direct-current triboelectric nanogenerator, *Adv. Funct. Mater.*, 2020, **30**, 2002547.

14 D. Z. Zhang, Z. Y. Xu, Z. M. Yang and X. S. Song, High-performance flexible self-powered tin disulfide nanoflowers/reduced graphene oxide nanohybrid-based humidity sensor driven by triboelectric nanogenerator, *Nano Energy*, 2020, **67**, 104251.

15 K. Kwon, J. U. Kim, Y. J. Deng, S. R. Krishnan, J. Choi, H. Jang, K. H. Lee, C. J. Su, I. Yoo, Y. X. Wu, L. Lipschultz, J. H. Kim, T. S. Chung, D. R. Wu, Y. Park, T. I. Kim, R. Ghaffari, S. Lee, Y. G. Huang and J. A. Rogers, An on-skin platform for wireless monitoring of flow rate, cumulative loss and temperature of sweat in real time, *Nat. Electron.*, 2021, **4**, 302–312.

16 H. Wu, Z. K. Wang and Y. L. Zi, Multi-mode water-tube-based triboelectric nanogenerator designed for low-frequency energy harvesting with ultrahigh volumetric charge density, *Adv. Energy Mater.*, 2021, **11**, 2100038.

17 Y. Wang, X. Y. Liu, T. Y. Chen, H. Wang, C. Q. Zhu, H. Y. Yu, L. G. Song, X. X. Pan, J. C. Mi, C. Lee and M. Y. Xu, An underwater flag-like triboelectric nanogenerator for harvesting ocean current energy under extremely low velocity condition, *Nano Energy*, 2021, **90**, 106503.

18 Y. J. Su, J. J. Wang, B. Wang, T. N. Yang, B. X. Yang, G. Z. Xie, Y. H. Zhou, S. L. Zhang, H. L. Tai, Z. X. Cai, G. R. Chen, Y. D. Jiang, L. Q. Chen and J. Chen, Alveolus-inspired active membrane sensors for self-powered wearable chemical sensing and breath analysis, *ACS Nano*, 2020, **14**, 6067–6075.

19 S. Wang, G. Z. Xie, H. L. Tai, Y. J. Su, B. X. Yang, Q. P. Zhang, X. S. Du and Y. D. Jiang, Ultrasensitive flexible self-powered ammonia sensor based on triboelectric nanogenerator at room temperature, *Nano Energy*, 2018, **51**, 231–240.

20 S. Wang, B. H. Liu, Z. H. Duan, Q. N. Zhao, Y. J. Zhang, G. Z. Xie, Y. D. Jiang, S. R. Li and H. L. Tai, PANI nanofibers-supported Nb$_2$CT$_x$ nanosheets-enabled selective $NH_3$ detection driven by TENG at room temperature, *Sens. Actuators, B*, 2021, **327**, 128923.

21 Y. J. Su, T. N. Yang, X. Zhao, Z. X. Cai, G. R. Chen, M. L. Yao, K. L. Chen, M. Bick, J. J. Wang, S. D. Li, G. Z. Xie, H. L. Tai, X. S. Du, Y. D. Jiang and J. Chen, A wireless energy

This journal is © The Royal Society of Chemistry 2022

*J. Mater. Chem. A*, 2022, **10**, 10935–10949 | **10947**

transmission enabled wearable active acetone biosensor for non-invasive prediabetes diagnosis, *Nano Energy*, 2020, **74**, 104941.

22 Z. H. Zhao, L. L. Zhou, S. X. Li, D. Liu, Y. H. Li, Y. K. Gao, Y. B. Liu, Y. J. Dai, J. Wang and Z. L. Wang, Selection rules of triboelectric materials for direct-current triboelectric nanogenerator, *Nat. Commun.*, 2021, **12**, 4686.

23 J. N. Kim, J. Lee, T. W. Go, A. Rajabi-Abhari, M. Mahato, J. Y. Park, H. Lee and I. K. Oh, Skin-attachable and biofriendly chitosan-diatom triboelectric nanogenerator, *Nano Energy*, 2020, **75**, 104904.

24 R. Z. Pan, W. P. Xuan, J. K. Chen, S. R. Dong, H. Jin, X. Z. Wang, H. L. Li and J. K. Luo, Fully biodegradable triboelectric nanogenerators based on electrospun polylactic acid and nanostructured gelatin films, *Nano Energy*, 2018, **45**, 193–202.

25 Q. Z. Sun, L. Wang, X. P. Yue, L. R. Zhang, G. Z. Ren, D. H. Li, H. C. Wang, Y. J. Han, L. L. Xiao, G. Lu, H. D. Yu and W. Huang, Fully sustainable and high-performance fish gelatin-based triboelectric nanogenerator for wearable movement sensing and human-machine interaction, *Nano Energy*, 2021, **89**, 106329.

26 Y. J. Han, Y. F. Han, X. P. Zhang, L. Li, C. W. Zhang, J. H. Liu, G. Lu, H. D. Yu and W. Huang, Fish gelatin based triboelectric nanogenerator for harvesting biomechanical energy and self-powered sensing of human physiological signals, *ACS Appl. Mater. Interfaces*, 2020, **12**, 16442–16450.

27 C. M. Jiang, C. Wu, X. J. Li, Y. Yao, L. Y. Lan, F. N. Zhao, Z. Z. Ye, Y. B. Ying and J. F. Ping, All-electrospun flexible triboelectric nanogenerator based on metallic MXene nanosheets, *Nano Energy*, 2019, **59**, 268–276.

28 W. X. Zhang, Y. Zhang, G. Z. Yang, X. Y. Hao, X. Lv, F. Wu, J. L. Liu and Y. H. Zhang, Wearable and self-powered sensors made by triboelectric nanogenerators assembled from antibacterial bromobutyl rubber, *Nano Energy*, 2021, **82**, 105769.

29 X. X. Shi, S. D. Zhang and S. Q. Gong, A self-powered and arch-structured triboelectric nanogenerator for portable electronics and human-machine communication, *J. Mater. Chem. A*, 2020, **8**, 8997–9005.

30 H. Q. Wang, J. Y. Wang, R. J. Liao, L. J. Yang, H. Wu and Z. L. Wang, Detrapping current measurement system driven by triboelectric nanogenerators for mapping electron trap states in dielectrics, *Adv. Funct. Mater.*, 2021, **31**, 2103463.

31 L. Q. Zhang, X. J. Li, Y. L. Zhang, Y. G. Feng, F. Zhou and D. Wang, Regulation and influence factors of triboelectricity at the solid-liquid interface, *Nano Energy*, 2020, **78**, 105370.

32 Q. Q. Shen, X. K. Xie, M. F. Peng, N. Sun, H. Y. Shao, H. C. Zheng, Z. Wen and X. H. Sun, Self-powered vehicle emission testing system based on coupling of triboelectric and chemoresistive effects, *Adv. Funct. Mater.*, 2018, **28**, 1703420.

33 K. Q. Xia, D. Wu, J. M. Fu, N. A. Hoque, Y. Ye and Z. W. Xu, Tunable output performance of triboelectric nanogenerator based on alginate metal complex for sustainable operation of intelligent keyboard sensing system, *Nano Energy*, 2020, **78**, 105263.

34 T. H. Chang, Y. W. Peng, C. H. Chen, T. W. Chang, J. M. Wu, J. C. Hwang, J. Y. Gan and Z. H. Lin, Protein-based contact electrification and its uses for mechanical energy harvesting and humidity detecting, *Nano Energy*, 2016, **21**, 238–246.

35 B. X. Zhang, F. D. Qu, X. X. Zhou, S. D. Zhang, T. Thomas and M. H. Yang, Porous coral-like $NiCo_2O_4$ nanospheres with promising xylene gas sensing properties, *Sens. Actuators, B*, 2018, **261**, 203–209.

36 Y. Y. Zheng, L. Q. Wang, H. W. Tian, L. Qiao, Y. Zeng and C. B. Liu, Bimetal carbonaceous templates for multi-shelled $NiCo_2O_4$ hollow sphere with enhanced xylene detection, *Sens. Actuators, B*, 2021, **339**, 129862.

37 M. He, L. L. Xie, G. F. Luo, Z. H. Li, J. Wright and Z. G. Zhu, Flexible fabric gas sensors based on $PANI/WO_3$ p–n heterojunction for high performance $NH_3$ detection at room temperature, *Sci. China Mater.*, 2020, **63**, 2028–2039.

38 S. Q. Li, A. Liu, Z. J. Yang, J. M. He, J. Wang, F. M. Liu, H. Y. Lu, X. Yan, P. Sun, X. S. Liang, Y. Gao and G. Y. Lu, Room temperature gas sensor based on tin dioxide@polyaniline nanocomposite assembled on flexible substrate: ppb-level detection of $NH_3$, *Sens. Actuators, B*, 2019, **299**, 126970.

39 X. W. Wang, L. K. Gong, D. Z. Zhang, X. X. Fan, Y. B. Jin and L. Guo, Room temperature ammonia gas sensor based on polyaniline/copper ferrite binary nanocomposites, *Sens. Actuators, B*, 2020, **322**, 128615.

40 X. Y. Yang, X. J. Yu, Q. Yang, D. L. Zhao, K. Zhang, J. X. Yao, G. Li, H. D. Zhou and X. Q. Zuo, Controllable synthesis and magnetic properties of hydrothermally. synthesized $NiCo_2O_4$ nano-spheres, *Ceram. Int.*, 2017, **43**, 8585–8589.

41 J. Tan, S. Hussain, C. X. Ge, M. S. Wang, S. Shah, G. W. Liu and G. J. Qiao, ZIF-67 MOF-derived unique double-shelled $Co_3O_4/NiCo_2O_4$ nanocages for superior gas-sensing performances, *Sens. Actuators, B*, 2020, **303**, 127251.

42 F. Dang, Y. L. Wang, J. N. Gao, L. P. Xu, P. F. Cheng, L. Lv, B. Zhang, X. Li and C. Wang, Hierarchical flower-like $NiCo_2O_4$ applied in n-butanol detection at low temperature, *Sens. Actuators, B*, 2020, **320**, 128577.

43 X. Li, J. L. Xu, Y. D. Jiang, Z. Z. He, B. H. Liu, H. K. Xie, H. Li, Z. M. Li, Y. Wang and H. L. Tai, Toward agricultural ammonia volatilization monitoring: A flexible polyaniline/ $Ti_3C_2T_x$ hybrid sensitive films based gas sensor, *Sens. Actuators, B*, 2020, **316**, 128144.

44 J. J. Bian, X. P. Cheng, X. Y. Meng, J. Wang, J. G. Zhou, S. Q. Li, Y. F. Zhang and C. W. Sun, Nitrogen-doped $NiCo_2O_4$ microsphere as an efficient catalyst for flexible rechargeable zinc-air batteries and self-charging power system, *ACS Appl. Energy Mater.*, 2019, **2**, 2296–2304.

45 S. W. Cui, Y. B. Zheng, T. T. Zhang, D. A. Wang, F. Zhou and W. M. Liu, Self-powered ammonia nanosensor based on the integration of the gas sensor and triboelectric nanogenerator, *Nano Energy*, 2018, **49**, 31–39.

46 S. Wang, H. L. Tai, B. H. Liu, Z. H. Duan, Z. Yuan, H. Pan, Y. J. Su, G. Z. Xie, X. S. Du and Y. D. Jiang, A facile

**10948** | *J. Mater. Chem. A*, 2022, **10**, 10935–10949

This journal is © The Royal Society of Chemistry 2022

respiration-driven triboelectric nanogenerator for multifunctional respiratory monitoring, *Nano Energy*, 2019, **58**, 312–321.

47 Y. Yang, D. Z. Zhang, D. Y. Wang, Z. Y. Xu and J. H. Zhang, A high-stability weighing paper/polytetrafluoroethylene-based triboelectric nanogenerator for self-powered $In_2O_3$ nanocubes/$SnS_2$ nanoflower $NO_2$ gas sensors, *J. Mater. Chem. A*, 2021, **9**, 14495–14506.

48 D. Z. Zhang, Z. M. Yang, S. J. Yu, Q. Mi and Q. N. Pan, Diversiform metal oxide-based hybrid nanostructures for gas sensing with versatile prospects, *Coord. Chem. Rev.*, 2020, **413**, 213272.

49 D. Duan, J. P. Ye and K. Li, Ni-Co-LDH and Zn-Co prussian blue analogue derived hierarchical $NiCo_2O_4$@ZnO/$ZnCo_2O_4$ microspheres with enhanced electrochemical sensing performance towards pentachloronitrobenzene, *Sens. Actuators, B*, 2021, **344**, 130222.

50 A. Sharma, P. Bhojane, A. K. Rana, Y. Kumar and P. M. Shirage, Mesoporous nickel cobalt hydroxide/oxide as an excellent room temperature ammonia sensor, *Scr. Mater.*, 2017, **128**, 65–68.

51 X. Dong, X. L. Cheng, X. F. Zhang, L. L. Sui, Y. M. Xu, S. Gao and H. Zhao, A novel coral-shaped $Dy_2O_3$ gas sensor for high sensitivity $NH_3$ detection at room temperature, *Sens. Actuators, B*, 2018, **255**, 1308–1315.

52 Y. P. Liu, Y. B. Zheng, Z. S. Wu, L. Q. Zhang, W. X. Sun, T. H. Li, D. A. Wang and F. Zhou, Conductive elastic sponge-based triboelectric nanogenerator (TENG) for effective random mechanical energy harvesting and ammonia sensing, *Nano Energy*, 2021, **79**, 105422.

53 G. Wang, S. J. Yang, L. Cao, P. K. Jin, X. K. Zeng, X. W. Zhang and J. Wei, Engineering mesoporous semiconducting metal oxides from metal-organic frameworks for gas sensing, *Coord. Chem. Rev.*, 2021, **445**, 214086.

54 H. Y. Tang, L. N. Sacco, S. Vollebregt, H. Y. Ye, X. J. Fan and G. Q. Zhang, Recent advances in 2D/nanostructured metal sulfide-based gas sensors: mechanisms, applications, and perspectives, *J. Mater. Chem. A*, 2020, **8**, 24943–24976.

55 M. Yang, X. F. Zhang, C. Y. Guo, X. L. Cheng, C. H. Zhu, Y. M. Xu, Z. Major and L. H. Huo, Resistive room temperature DMA gas sensor based on the forest-like unusual n-type PANI/$TiO_2$ nanocomposites, *Sens. Actuators, B*, 2021, **342**, 130067.

56 Q. Chen, Y. H. Zhang, S. Y. Ma, Y. H. Wang, P. Y. Wang, G. H. Zhang, D. J. Gengzang, H. Y. Jiao, M. X. Wang and W. J. Chen, Multishelled NiO/$NiCo_2O_4$ hollow microspheres derived from bimetal-organic frameworks as high-performance sensing material for acetone detection, *J. Hazard. Mater.*, 2021, **415**, 125662.

57 D. Z. Zhang, Z. M. Yang, Z. L. Wu and G. K. Dong, Metal-organic frameworks-derived hollow zinc oxide/cobalt oxide nanoheterostructure for highly sensitive acetone sensing, *Sens. Actuators, B*, 2019, **283**, 42–51.

58 H. Wang, Y. Y. Luo, B. Liu, L. Gao and G. T. Duan, CuO nanoparticle loaded ZnO hierarchical heterostructure to boost $H_2S$ sensing with fast recovery, *Sens. Actuators, B*, 2021, **338**, 129806.

59 D. Meng, D. Y. Liu, G. S. Wang, Y. B. Shen, X. G. San, M. Li and F. L. Meng, Low-temperature formaldehyde gas sensors based on NiO-$SnO_2$ heterojunction microflowers assembled by thin porous nanosheets, *Sens. Actuators, B*, 2018, **273**, 418–428.

60 J. M. Suh, W. Sohn, Y. S. Shim, J. S. Cho, Y. G. Song, T. L. Kim, J. M. Jeon, K. C. Kwon, K. S. Choi, C. Y. Kang, H. G. Byun and H. W. Jang, P-P heterojunction of nickel oxide-decorated cobalt oxide nanorods for enhanced sensitivity and selectivity toward volatile organic compounds, *ACS Appl. Mater. Interfaces*, 2018, **10**, 1050–1058.

This journal is © The Royal Society of Chemistry 2022

*J. Mater. Chem. A*, 2022, **10**, 10935–10949 | **10949**